

# Polarization-Wavelength Locked Plasmonic Topological States

Yuanzhen Li<sup>1, 2</sup>, Zijian Zhang<sup>1, 2</sup>, Hongsheng Chen<sup>1, 2</sup>, and Fei Gao<sup>1, 2, \*</sup>

**Abstract**—Plasmonic topological states, providing a new way to bypass the diffraction limits and against fabrication disorders, have attracted intense attention. In addition to the near-field coupling and band topology, the localized surface plasmonic resonance modes can be manipulated with far-field degrees of freedom (DoFs), such as polarization. However, changing the frequency of the topological edge states with different polarized incident waves remains a challenge, which has led to significant interest in multiplexed radiative topological devices. Here, we report the realization of polarization-wavelength locked plasmonic topological edge states on the Su-Schrieffer-Heeger (SSH) model. We theoretically and numerically show that such phenomenon is based on two mechanisms, i.e., the splitting in the spectra of plasmonic topological edge states with different intrinsic parity DoF and projecting the far-field polarizations to the parity of lattice modes. These results promise applications in robust optical emitters and multiplexed photonic devices.

## 1. INTRODUCTION

Plasmonic systems [1, 2], which possess features such as subwavelength field confinement and resulting enhancement, bypass the diffraction limits and have gained significant interest in various applications, including optical antenna, surface-enhance Raman scattering, biological sensors, harmonic generation, and superlenses [2]. However, localized surface plasmonic resonance modes on small metallic particles are prone to serious backscattering caused by fabrication disorders. To address this issue, a strategy to protect against fabrication disorder is to push topological physics into photonics and plasmonics.

Topological photonics/plasmonics [3–7] applies the principles of topological physics to the study of light to manipulate the flow of photons in specially designed materials and structures. These materials, known as topological insulators, have unique properties that protect light waves from scattering or diffraction, even when the material has defects or is subject to disturbances. This protection is achieved through the guidance of light waves by topologically protected edge states, which are robust against various perturbations. The Su-Schrieffer-Heeger (SSH) model is a simple topologically nontrivial model that features a one-dimensional (1D) chain of atoms with staggered hopping [8–13]. In the field of plasmonics, two analogous systems exist [14–27]: a straight chain of metallic nanoparticles with alternating spacing [14–16] and a zig-zag chain [17–20, 27].

In addition to the near-field coupling and band topology, the localized surface plasmonic resonance modes can be manipulated with far-field degrees of freedom (DoFs), such as polarization. In a zig-zag nanoparticle chain, the interaction among induced dipole resonances strongly depends on the dipole orientation, which is determined by the polarization direction of the normally-illuminated wave [2, 17–19]. This provides a feasible way to tune the position of topological edge states without adjusting the structure parameters. However, changing the frequency of the topological edge states with different

---

*Received 10 August 2023, Accepted 17 September 2023, Scheduled 25 September 2023*

\* Corresponding author: Fei Gao (gaofezju@zju.edu.cn).

<sup>1</sup> Interdisciplinary Center for Quantum Information, State Key Laboratory of Modern Optical Instrumentation, College of Information Science and Electronic Engineering, Zhejiang University, Hangzhou 310027, China. <sup>2</sup> International Joint Innovation Center, Key Laboratory of Advanced Micro/Nano Electronic Devices & Smart Systems of Zhejiang, The Electromagnetics Academy at Zhejiang University, Zhejiang University, Haining 314400, China.

polarized incident waves remains a challenge, which has led to intense interest in multiplexed radiative topological devices [28–31].

Here, we demonstrate the realization of polarization-wavelength locked plasmonic topological edge states on the 1D SSH model, as shown in Fig. 1(a). As shown in Fig. 1(d), the topological edge states with even (odd) parity are pinned at 6.22 GHz (6.19 GHz) under a horizontal (vertical) linear-polarized illumination. This phenomenon is accounted for by that the topological edge states of specific mode parity are pinned to specific wavelengths, and the mode parities are one-to-one mapped to the polarizations of far-field waves. We term this phenomenon as polarization-wavelength locking for short. This phenomenon is based on two factors: (i) splitting in the spectra of plasmonic topological edge states with different intrinsic parity DoF and (ii) projecting the far-field polarizations to the parity of lattice modes. The parity splitting originates from the underlying inter-orbital couplings. The SSH model is realized using ultrathin spoof plasmonic resonators, as shown in the inset of Fig. 1(b). Spoof Surface plasmons mimic natural plasmonic materials in microwave and Terahertz regions, and they have similar behaviors [32–39]. The resonance peak at  $\omega_h = 6.069$  GHz is the focus of our study, which corresponds to the hexapole mode (as shown in the insets of Fig. 1(c)). Three crucial features of the hexapole mode distinguish the spoof plasmonic topological edge states from previous demonstrations: Firstly, the hexapole mode has two degenerate modes with even and odd parities, giving rise to two copies of parity-dependent topological edge states [12]. Secondly, the hexapole mode exhibits spectrally overlapping, which induces effective parity-dependent in-line long-range couplings and leads to the parity splitting of topological edge states. This fundamentally differs from the dipole-dipole long-range coupling observed in the zig-zag chains. Finally, the plasmonic resonance modes exhibit non-Hermiticity,

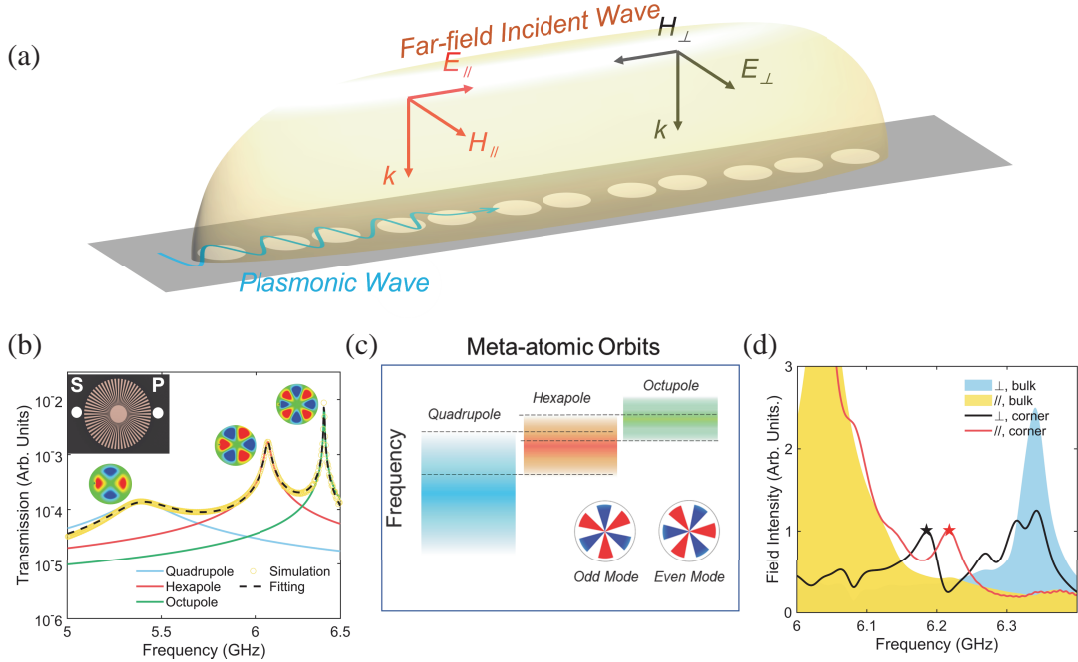


**Figure 1.** (a) The schematic of polarization-wavelength locked topological edge states on a plasmonic SSH chain. “//” and “ $\perp$ ” donates horizontal and vertical incident wave, respectively. (b) The near-field transmission spectrum of a single spoof plasmonic resonator. The inset shows the schematic, where the inner and out radii are  $r = 3$  mm, and  $R = 12$  mm, respectively. The groove number is  $N = 60$ , and the filling ratio is  $FR = 50\%$ . The points “S” and “P” denote the locations of the source and probe, respectively. The yellow circles and black dashed lines are simulated and Lorenz-curve-fitted results, respectively. The red, green, and blue denote quadrupole, hexapole, and octupole modes. (c) The overlapping between resonance modes in (b). The inset shows the hexapole modes with different parities. (d) Simulated field intensity at the edge and bulk resonator. The sample is normally incident waves with different linear polarizations.

which establishes a link between the far-field polarization and the near-field parity, allowing for the polarization-wavelength locking of the parity-dependent topological edge states.

## 2. ANALYSIS

### 2.1. Coupling between Resonators

We first show the intrinsic chiral symmetry of parity DoF by investigating the coupling of hexapole modes in a dimer system [35]. A spoof plasmonic dimer is shown in the inset of Fig. 2(a). The two adjacent plasmonic resonators are coupled with evanescent waves since they host tightly localized plasmonic modes. Quantitatively, such coupling is described with a coupling factor  $\kappa$ , which depends on the integration of overlapped resonance wave fields of the two resonators [40]. When taking interorbital coupling into consideration, there would appear an onsite-detuning to each resonance mode [41]. As a result, the coupled hexapole modes on the plasmonic dimer can be generally described with the effective Hamiltonian  $\hat{H}_{\text{dimer}} = \omega_h + \begin{bmatrix} -\Delta\omega_{\text{eff}} & \kappa_h \\ \kappa_h & -\Delta\omega_{\text{eff}} \end{bmatrix}$ , where  $\omega_h$  is the frequency of hexapole mode in each resonator,  $\kappa_h$  the coupling coefficient between hexapole modes, and  $\Delta\omega_{\text{eff}}$  the effective on-site detuning (EOD). The dimer system exhibits two supermodes  $\phi_{\pm} = (1/\sqrt{2})[1, \pm 1]^T$ , corresponding to eigenfrequencies  $\omega_+ = \omega_h - \Delta\omega_{\text{eff}} + \kappa_h$ ,  $\omega_- = \omega_h - \Delta\omega_{\text{eff}} - \kappa_h$ , respectively. The sign  $+/-$  donates in-phase/out-of-phase, respectively. When the frequency  $\omega_+$  of the in-phase supermode  $\phi_+$  is higher (lower) than that of the out-of-phase one  $\phi_-$ , the dimer system exhibits a positive (negative) coupling  $\kappa_h$ . The EOD  $\Delta\omega_{\text{eff}} = -(\bar{\omega} - \omega_h)$  measures the shift of the average frequency  $\bar{\omega} = (\omega_+ + \omega_-)/2$ , with respect to the  $\omega_h$ .

The analysis above shows the parity-dependent of both  $\Delta\omega_{\text{eff}}$  and  $\kappa_h$ . In the spoof plasmonic dimer, the even (odd) hexapole mode is selectively excited by end (side) excitation as shown in the inset of Fig. 2(a), and the corresponding spectrum is shown as the red (black) line in Fig. 2(a). Regarding the even (odd) hexapole mode, the dimer system exhibits an in-phase supermode at a frequency lower (higher) than that of out-of-phase one (shown in Fig. 2(b)). It means that parity-dependent couplings are  $\kappa_{h,o} > 0$  and  $\kappa_{h,e} < 0$ , where the subscripts “e” and “o” denote the even and odd modes respectively. The average frequency  $\bar{\omega}_{h,e}$  ( $\bar{\omega}_{h,o}$ ) of the even (odd) supermodes blueshift (redshift) concerning  $\omega_h$ . It means that the EOD  $\Delta\omega_{\text{eff}}$  exhibits the same parity-dependence as  $\kappa_h$ . Consequently, these sign-reversed interactions imply that the dimer Hamiltonian should be completely expressed as

$\hat{H}_{\text{dimer}} = \omega_h + \begin{bmatrix} -\Delta\omega_{\text{eff}} & \kappa_h \\ \kappa_h & -\Delta\omega_{\text{eff}} \end{bmatrix} \otimes \sigma_z$ , where  $\sigma_z$  represents the Pauli matrix for the parity DoF. We theoretically find that the origin of EOD can be attributed to the interorbital coupling between the hexapole mode and its neighboring quadrupole modes and octupoles due to their spectral overlapping.

To directly display the interorbital coupling, we take a straight plasmonic trimer for illustration (as shown in the inset of Fig. 2(c)). We consider first the trimer model without interorbital couplings, thus only couplings between hexapole modes (i.e., hexapole-hexapole-hexapole coupling). The trimer

Hamiltonian is expressed as  $\hat{H}_{\text{trimer},0} = \omega_h + \begin{bmatrix} 0 & \kappa_h & 0 \\ \kappa_h & 0 & \kappa_h \\ 0 & \kappa_h & 0 \end{bmatrix}$ , without considering the parity DoF. Three

eigenfrequencies are obtained as  $\omega_{1,3} = \omega_h \mp \sqrt{2}\kappa_h$ ,  $\omega_2 = \omega_h$ . Interestingly, the middle eigenfrequency  $\omega_2$  does not depend on  $\kappa_h$ , which means for both even ( $\kappa_{h,e} < 0$ ) and odd ( $\kappa_{h,o} > 0$ ) modes, the middle eigenfrequencies  $\omega_{2,e}$  and  $\omega_{2,o}$  are degenerate and pinned at  $\omega_h$ . Both  $\omega_{2,e}$  and  $\omega_{2,o}$  correspond to the supermode  $[A_L, A_M, A_R]^T = 1/\sqrt{2}[1, 0, 1]^T$ , where  $A_{L,M,R}$  denote lattice modes on the left, middle, and right resonators, respectively. Different from the vanished  $A_M$  in the hexapole-hexapole-hexapole coupling model, the simulated field pattern (Fig. 2(d)) shows nonvanishing fields. By mode decomposing, the simulated  $A_M$  is a superposition of quadrupole and octupole modes. It implies that the interorbital couplings (i.e., hexapole-quadrupole-hexapole, and hexapole-octupole-hexapole) do exist.

The interorbital coupling, effectively expressed as  $\hat{H}_{\text{trimer},\text{IOC}} = \begin{bmatrix} -\Delta\omega & 0 & \kappa_3 \\ 0 & -2\Delta\omega & 0 \\ \kappa_3 & 0 & -\Delta\omega \end{bmatrix}$  results

in a modified trimer Hamiltonian  $\hat{H}_{\text{trimer}} = (\hat{H}_{\text{trimer},0} + \hat{H}_{\text{trimer},\text{IOC}})$ , where  $\kappa_3$  and  $\Delta\omega$  represent the

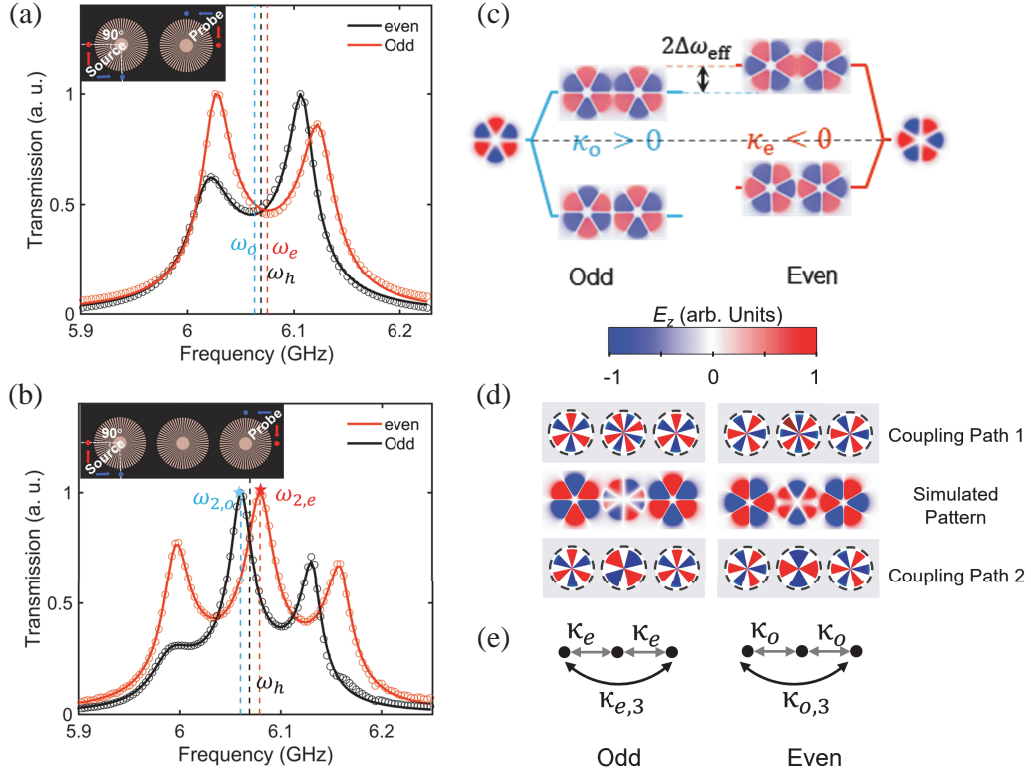


**Figure 2.** The parity-dependent couplings between plasmonic resonators. (a) The transmission spectra of a spoof plasmonic dimer with a center-to-center distance of 29 mm. The red and black lines are measured with the end and side excitations, respectively. The red ( $\omega_e$ ) and blue ( $\omega_o$ ) dashed lines indicate the average frequencies of two split resonance peaks. The black dashed line represents the frequency  $\omega_h$  of hexapole modes. The inset shows the schematic of the spoof plasmonic dimer. (b) The illustration of parity-dependent couplings in the spoof plasmonic dimer. The even and odd parities exhibit negative and positive couplings, respectively. (c) The transmission spectra of a spoof plasmonic trimer. The inset shows the schematic of the meta-trimer. (d) The field patterns for odd and even parities at  $\omega_{2,o}$  (the blue star in (c)) and  $\omega_{2,e}$  (the red star in (c)), respectively. The patterns on the middle metaatom are the superpositions of quadrupole modes and octupole modes. (e) The illustration of the effective long-range coupling induced by the interorbital coupling. a. u. is short for arbitrary units.

effective long-range coupling (Fig. 2(e)) and effective onsite detuning, respectively. Solving the modified Hamiltonian, we find that the middle eigenfrequency  $\omega_2 = \omega_h - \Delta\omega - \kappa_3$  shows a spectral shift with respect to  $\omega_h$ . Additionally, the average eigenfrequencies  $\bar{\omega} = (\omega_1 + \omega_3)/2 = (2\Delta\omega + \kappa_3)/2$ . So that the effective coupling coefficient can be expressed as  $\kappa_3 = (2\bar{\omega} - 3\omega_2)/4$ ,  $\Delta\omega = (2\bar{\omega} + \omega_2)/4$ . According to the spectral results in Fig. 2(c), the middle resonance peak of even ( $\omega_{2,e} = 6.079$  GHz) and odd ( $\omega_{2,o} = 6.060$  GHz) show blue- and red-shifts with respect to  $\omega_h$ . It means that the interorbital couplings are also parity dependent, i.e.,  $\kappa_{3,e} = -\kappa_{3,o}$ ,  $\Delta\omega_e = -\Delta\omega_o$ . Therefore, the trimer Hamiltonian

should be completely expressed as  $\hat{H}_{\text{trimer}} = \begin{bmatrix} -\Delta\omega & \kappa_h & \kappa_3 \\ \kappa_h & -2\Delta\omega & \kappa_h \\ \kappa_3 & \kappa_h & -\Delta\omega \end{bmatrix} \otimes \sigma_z$ . The effective long-range

coupling originates from spectral overlapping of neighboring modes, essentially different from direct long-range coupling induced by dipole-dipole interactions. And the long-range coupling is realized in the straight trimer system, which can help make the lattice more compact.

## 2.2. SSH Model with Parity Multiplexing and Long-Range Coupling

Based on the microscopic analysis above, we can abstract the spoof plasmonic SSH chain in Fig. 1 as the models shown in Fig. 1(c), where  $\pm\kappa_1$ ,  $\pm\kappa_2$ , and  $\pm\kappa_3$  represent the intracell coupling, intercell coupling, and the effective long-range coupling, respectively. Its Hamiltonian is expressed as

$$\hat{H}_{\text{SSH}} = \hat{H}_{\text{SSH},0} \otimes \sigma_z + \hat{H}_{\text{SSH},\text{LRC}} \otimes \sigma_z \quad (1)$$

where  $\hat{H}_{\text{SSH},0} = \omega_h + \begin{bmatrix} 0 & \kappa_2 + \kappa_1 e^{ikd} \\ \kappa_2 + \kappa_1 e^{-ikd} & 0 \end{bmatrix}$  is the Hamiltonian of conventional SSH model, and the  $\hat{H}_{\text{SSH},\text{LRC}} = \begin{bmatrix} 2\kappa_3 \cos(kd) - \Delta\omega & 0 \\ 0 & 2\kappa_3 \cos(kd) - \Delta\omega \end{bmatrix}$ . The energy dispersion is given by  $E_{\text{SSH},\pm} = 2\kappa_3 \cos(kd) \pm \sqrt{\kappa_1^2 + \kappa_2^2 + 2\kappa_1\kappa_2 \cos(kd)}$ . This expression clarifies that the long-range couplings break the chiral symmetry, translating into an asymmetric band structure about  $E = 0$  [42, 43].

The topological properties of the SSH model can be described with the winding number  $\mathcal{W} = \frac{-i}{2\pi} \int_0^{2\pi} dk \frac{h'(k)}{h(k)}$ , where  $h(k) = \kappa_2 + \kappa_1 e^{ikd}$ . For the conventional SSH model, when  $\kappa_1 < \kappa_2$  ( $\kappa_1 > \kappa_2$ ),  $\mathcal{W} = 1$  ( $\mathcal{W} = 0$ ), the system is in topological (trivial) phase. Moreover, for the SSH model with long-range coupling, the properties of the system in the topological phase can be divided into two regimes: (i) When  $\kappa_3 < \kappa_1/2$ , the system has insulating properties and the bandgap exists. The winding number is still defined by the ratio  $\kappa_1/\kappa_2$  and corresponds to the number of edge states. (ii) When  $\kappa_3 > \kappa_1/2$ , the system behaves like metal and direct bandgap disappear. However, in this regime, the maximum of the valence band is at  $k = 0$  while the minimum of the conduction band is at  $k = \pi$ , i.e., the energy bands do not cross, which implies there is no topological phase transition.

To understand the influence of parity multiplexing and long-range coupling on topological edge states, we start from a finite conventional SSH chain with the intracell coupling  $\kappa_1$  and intercell coupling  $\kappa_2$  as Fig. 3(a) shows. When  $\kappa_1 < \kappa_2$ , the topological edge states (black lines in Fig. 3(d)) exist in the bandgap and are pinned at zero frequency (i.e.,  $\omega_h$ ) while when  $\kappa_1 > \kappa_2$  the topological edge states disappear. By introducing the parity multiplexing into consideration as Fig. 3(b) and Fig. 3(e) show, the edge states with different parity are degenerate at zero frequency  $\omega_h$  in the topological phase ( $\kappa_1 < \kappa_2$ ). And then, we apply the long-range couplings as Fig. 3(c) and 3(f) show. With the increasing of long-range coupling  $\kappa_3$ , the topological corner states with different parities split. In Fig. 3(f), the red (black) lines indicate that the energies of edge states with even (odd) parity blue- (red-) shift with the increasing of  $\kappa_3$ . When  $\kappa_3/\kappa_1 > 0.18$ , the even (odd) edge states overlap with odd (even) bulk states in spectra. However, they can be distinguished through selective excitation. It is also noteworthy that in the system where the long-range coupling and EOD exist, the topological edge states at different ends of the chain are degenerate, unlike the nondegenerate end states induced by asymmetrical onsite detuning [13].

## 3. RESULTS AND DISCUSSION

The theoretical analysis above can be applied in the spoof plasmonic SSH chain, as Fig. 4(a) shows. Here, we use the full-wave approach to numerically examine the properties of spoof plasmonic SSH chain. The sample can be realized by printing 18  $\mu\text{m}$  thick copper on a 0.254 mm thick RT/duroid 5880 (permittivity  $\epsilon = 2.2 \pm 0.01$ ; loss tangent  $\Delta\delta = 0.0009$ ) dielectric substrate. The geometric parameters of the resonator are as shown in Fig. 1(b). The distances between resonators are set as  $d_1 = 29$  mm and  $d_2 = 26$  mm, respectively. In Fig. 4(b), we show the numerically computed bulk bands for the infinite structure corresponding to the chain shown in Fig. 4(a), and though curve fitting the corresponding coupling coefficients can be extracted as  $\kappa_{1;e,o} = \pm 0.0297$ ,  $\kappa_{2;e,o} = \pm 0.0918$ , and  $\Delta\omega_{e,o} = \kappa_{3;e,o} = \mp 0.0031$ , respectively. With the introduction of effective long-range coupling and onsite detuning, the bands of even mode and odd mode are not degenerate. The two bands with the same parity are not symmetric about  $E = \omega_h$  because of the broken chiral symmetry. Applying the extracted coupling coefficients in a finite SSH chain with 14 sites shows the numerical calculated eigenfrequencies and eigenmodes in Fig. 4(c). In bandgap, two groups of edge states respond to the topological edge states with different parities, and the field intensity is highly localized at the edge resonators. Fig. 4(d) shows the local densities of even (odd) edge states detected at the A (B) point.

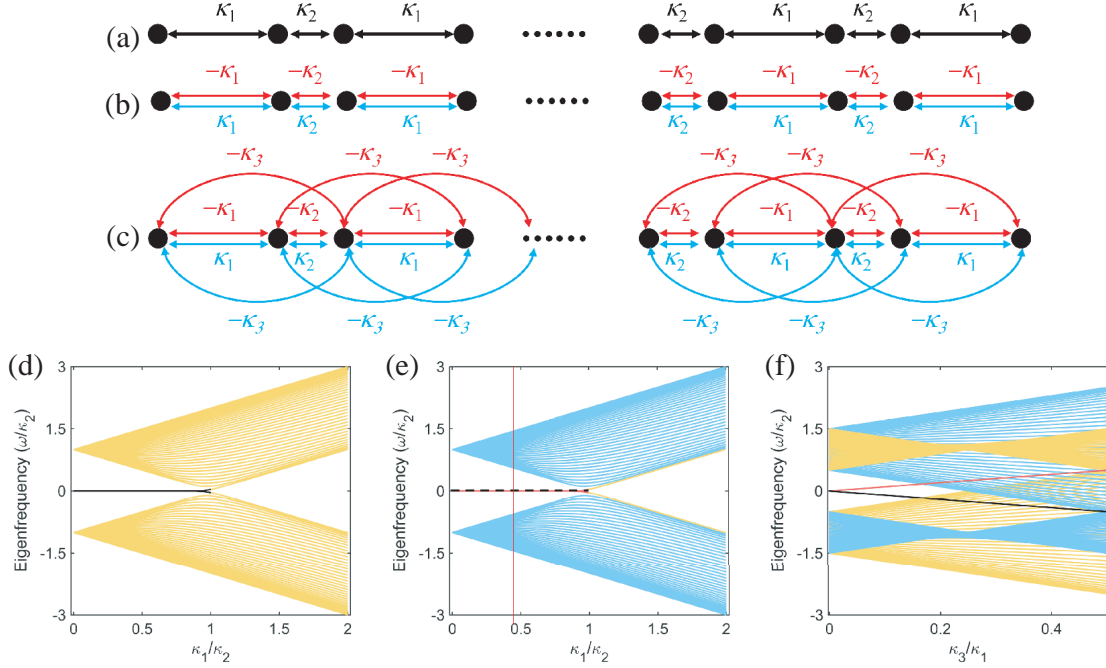


**Figure 3.** Effects of mode parity and long-range coupling on SSH model. (a) The schematic of conventional SSH chain. (b) The schematic of SSH chain with parity multiplexing. The coupling coefficients for the odd (even) mode are positive (negative). (c) The schematic of the SSH chain with both parity multiplexing and long-range coupling. (d) The energy spectrum of a finite conventional SSH chain (161 sites), with varying ratio  $\kappa_2/\kappa_1$ . (e) The energy spectrum of a finite SSH chain with parity multiplexing. (f) The energy spectrum of a finite SSH chain with both parity multiplexing and long-range couplings. The yellow (blue) lines show the bulk states with odd (even) parity, and the black (red) dashed lines show the bulk states with odd (even) parity, respectively. assuming  $\kappa_2 = 1$  and  $\omega_h = 0$ .

The spectra show dominated peaks at 6.147 GHz (red) and 6.122 GHz (black) for points A and B, respectively. When comparing with the localized densities of bulk states (yellow and blue regions in Fig. 4(d)), the topological edge states distribute in the bandgap. Near-field patterns further confirm the parity-dependent edge states. In Fig. 4(e), the edge resonator shows brighter odd hexapole modes at 6.122 GHz than those on other resonators. One even-parity edge state at 6.147 GHz is also demonstrated in Fig. 4(f). This is consistent with the theoretical results in Fig. 4(c).

Besides the near-field observations, the parity-dependent topological edge states in spoof plasmonic SSH chains can also be probed with far-field polarized illuminations. The fundamental reason is that the ultrathin spoof plasmonic resonator exhibits radiative non-Hermiticity, which imposes no effect on in-plane bulk topologies but opens radiation channels to observe the far-field response. The radiative non-Hermiticity can be described as  $\hat{H}_{\text{NH}} \otimes \sigma_0$ , where  $\hat{H}_{\text{NH}} = \begin{bmatrix} i\gamma_h & 0 \\ 0 & i\gamma_h \end{bmatrix}$  and  $\sigma_0$  represent identity matrix, and  $\gamma_h = 0.006$  represents the radiation loss of the hexapole mode. Since a diagonal and uniform Hamiltonian cannot change the bulk topologies, the topological edge states can still exist with the radiative non-Hermiticity. Fig. 5(a) shows the radiation pattern of an individual resonator excited by a near-field monopole at 6.069 GHz (i.e.,  $\omega_h$ ). The radiation of the hexapole mode consists of in-plane and out-of-plane parts, indicating the existence of radiative non-Hermiticity.

Unfortunately, the hexapole mode on the single resonator cannot be excited by a normally illuminated linear-polarized wave. Fig. 5(b) shows that only dipole mode can be excited. Interestingly, in a dimer system, the resonators can be normally excited by horizontal polarized ( $H$ -polarized, i.e., the electric field is parallel with the dimer axis) and vertical polarized ( $V$ -polarized, i.e., the electric

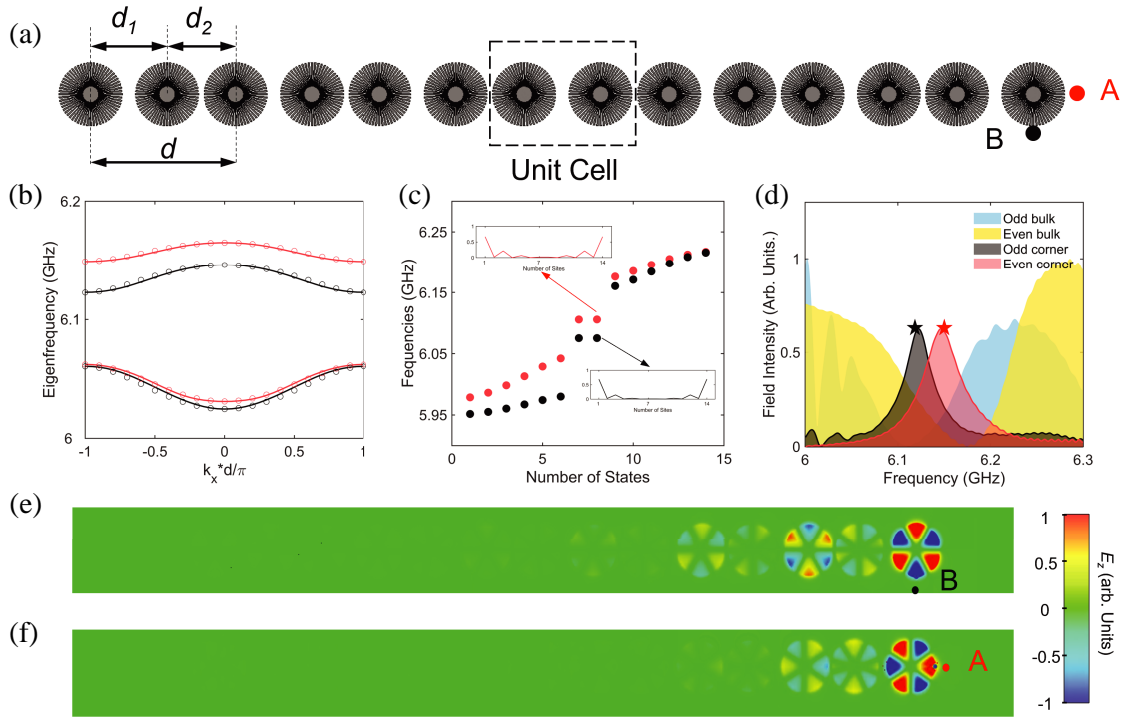


**Figure 4.** The near-field characteristic of parity-split topological edge states in spoof plasmonic SSH chain. (a) The schematic of the spoof plasmonic SSH chain.  $d_1$  and  $d_2$  represent the intracell and intercell distance, respectively. A and B points represent the exciting position for even and odd modes, respectively. (b) Simulated band energy of the SSH chain. (c) The Calculated eigen spectrum of different parities with  $\kappa_{1;o,e} = \pm 0.0297$ ,  $\kappa_{2;o,e} = \pm 0.0918$ ,  $\kappa_{3;o,e} = \mp 0.0031$ . The insets show filed strength distribution of the topological edge states. (d) The simulated local density of states. (e)–(f) The simulated near-filed patterns of topological edge states. The odd-parity edge state at 6.147 GHz is shown in (e), and even at 6.122 GHz is shown in (f).

field is perpendicular to the dimer axis) illuminations. Fig. 5(c) shows the total scattering cross-section of a spoof plasmonic dimer with  $H$ - (red line) and  $V$ - (black line) polarized incident wave. Due to the existence of a dipolar radiation spectrum, Fano resonances can be observed at 6.18 GHz and 6.28 GHz, i.e., the resonance frequencies of hexapole modes [44–46]. The two resonances correspond to even- and odd-parity supermodes, as shown in the insets of Fig. 5(c).

The correspondences between far-field polarizations and near-field parities can be explained through dipole decomposition as Figs. 5(d)–(e) shows [41]. In an individual resonator, the hexapole can be decomposed into three dipoles with the same strength, spaced at  $60^\circ$  intervals. Therefore, the total dipolar momentum vanishes. It implies the hexapole modes cannot be excited by the normal incident wave of the mismatching between the total dipolar momentum and the electric field of the incident wave. Nevertheless, in the coupled system, the strength of three composite dipoles would be unbalanced due to the perturbations from the neighboring resonators, which leads to the residual dipole and induces the matching with the electric field of the incident wave. Fig. 5(e) shows the dipolar decomposition of the supermodes in the dimer system. Note that only the symmetric supermodes (i.e.,  $\phi_+ = (1/\sqrt{2})[1, 1]^T$ ) own the nonzero residual dipole momentums.

Figure 5(f) shows the numerically calculated total scattering cross-section spectra for the structure in Fig. 4(a) with normal linear-polarized illumination. The bulk states in the symmetric phase have induced a considerable resonance against the continuum spectra of dipole modes. At the frequencies of topological edge states as marked in Fig. 4(f), the near-field pattern is shown in Figs. 4(g) and (h). This polarized illumination selection on parity-dependent topological edge states is consistent with both theoretical and near-field experimental results.

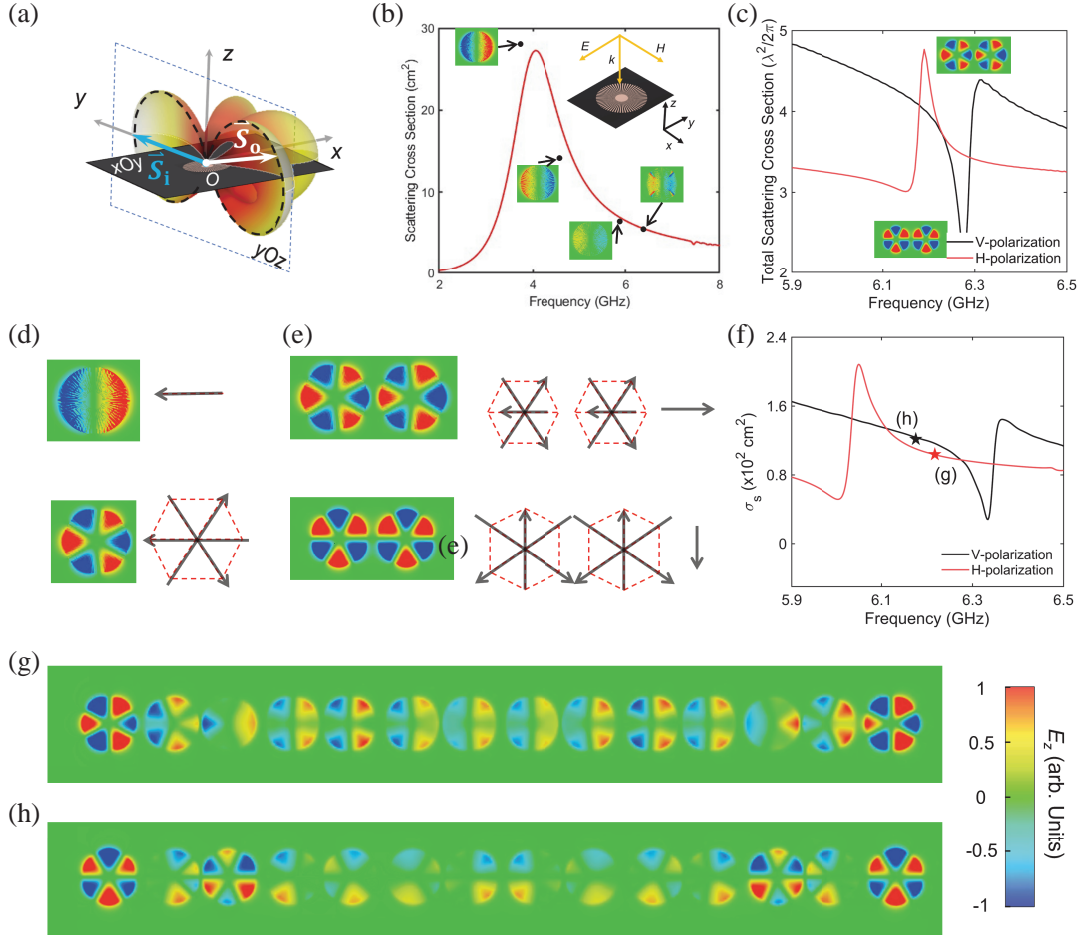


**Figure 5.** The far-field demonstration of polarization-wavelength locking of topological edge states. (a) The far-field radiation pattern of an individual resonator excited by a near-field monopole.  $S_i$  and  $S_o$  represent the in-plane and out-of-plane radiation of the hexapole mode, respectively. (b) Simulated total scattering cross-section of a single resonator. The sample is normally illuminated with linearly-polarized waves, as the inset shows. (c) Simulated scattering cross-section of the dimer illuminated with  $H$ -polarized wave (red line) and  $V$ -polarized wave (black line), respectively. (d) The dipolar compound of dipole mode and hexapole mode on a single resonator. (e) The polarization-parity correspondence of plasmonic dimer. (f) Simulated total scattering cross section with  $H$ - and  $V$ -polarized incident plane wave. (g)–(h) The simulated patterns of topological edge states at the frequencies in (f). (g) shows the even-parity edge state excited by  $H$ -polarized incidence and (h) for the odd parity by  $V$ -polarized incidence.

#### 4. CONCLUSION

In conclusion, we realized polarization-wavelength locked topological edge states on a spoof plasmonic metasurface. The parity is an intrinsic DoF and does not depend on any crystalline. Hence, intriguing topological physics could be anticipated by incorporating the parity into other 2D or 3D lattices and can act with more DoFs such as anti- $PT$  symmetry. In such spoof plasmonic systems, non-Hermitian coupling, which has been realized to observe anti- $PT$  phase transition [39], could also be implemented to interact with the long-range coupling. Such a platform would be promising for investigating many interesting non-Hermitian topological phenomena (such as the non-Hermitian skin effect [47–49]). Moreover, the parity of resonance modes could be manipulated by incorporating interorbital couplings originating from spectral overlapping between neighboring modes. Our results may promise applications in polarization-dependent topological lasing [29] and quantum emitters [30].



## ACKNOWLEDGMENT

This work was supported by the Key Research and Development Program of the Ministry of Science and Technology under Grants No. 2022YFA1404902, 2022YFA1404704, and 2022YFA1405200, the National Natural Science Foundation of China (NNSFC) under Grants No. 62171406, 11961141010 and 61901411, the Zhejiang Provincial Natural Science Foundation under Grants No. Z20F010018, National Key Laboratory Foundation No. 6142205200402, the Fundamental Research Funds for the Central Universities No. 2020XZZX002-15.

## REFERENCES

1. Maier, S. A., *Plasmonics: Fundamentals and Applications*, Springer, U. S., 2007.
2. Giannini, V., A. I. Fernandez-Dominguez, S. C. Heck, and S. A. Maier, "Plasmonic nanoantennas: Fundamental and their use in controlling the radiative properties of nanoemitters," *Chem. Rev.*, Vol. 111, 3888–3912, 2011.
3. Lu, L., J. D. Joannopoulos, and M. Spljadic, "Topological photonics," *Nature Photonics*, Vol. 8, 821–829, 2014.
4. Ozawa, T., H. M. Price, A. Amo, et al., "Topological photonics," *Rev. Mod. Phys.*, Vol. 91, 015006, 2019.
5. Shastri, K., M. I. Abdelrahman, and F. Monticone, "Nonreciprocal and topological plasmonics," *Photonics*, Vol. 8, 133, 2021.
6. Zhuang, W., X. Chen, and F. Ye, "Plasmonic topological insulators for topological nanophotonics," *Optics Letters*, Vol. 42, No. 20, 4063–4066, 2017.
7. Leykam, D. and L. Yuan, "Topological phases in ring resonators: Recent progress and future prospects," *Nanophotonics*, Vol. 9, 15, 4473–4487, 2020.
8. Su, W. P., J. R. Schrieffer, and A. J. Heeger, "Solitons in Polyacetylene," *Physical Review Letters*, Vol. 45, No. 25, 1979.
9. Malkova, N., I. Hromada, X. Wang, G. Bryant, and Z. Chen, "Observation of optical Shockley-like surface states in photonic superlattices," *Optics Letters*, Vol. 34, No. 11, 1633–1635, 2009.
10. Xiao, M., Z. Q. Zhang, and C. T. Chan, "Surface impedance and bulk band geometric phases in one-dimensional system," *Physical Review X*, Vol. 4, 021017, 2014.
11. Miert, G. V. and C. Ortix, "Excess charges as a probe of one-dimensional topological crystalline insulating phases," *Physical Review B*, Vol. 96, 235130, 2017.
12. Chen, T., Y. Yu, Y. Song, D. Yu, H. Ye, J. Xie, X. Shen, Y. Pan, and Q. Cheng, "Distinguishing the topological zero mode and Tamm mode in a microwave waveguide array," *Ann. Phys. (Berlin)*, Vol. 531, 1900347, 2019.
13. Li, G., L. Wang, R. Ye, Y. Zheng, D.-W. Wang, X.-J. Liu, A. Dutt, L. Yuan, and X. Chen, "Direct extraction of topological Zak phase with the synthetic dimension," *Light: Science & Applications*, Vol. 12, No. 1, 81, 2023.
14. Pockock, S. R., X. Xiao, P. A. Huidobro, and V. Giannini, "Topological plasmonic chain with retardation and radiative effects," *ACS Photonics*, Vol. 5, 2271–2279, 2018.
15. Compaijen, P. J., V. A. Malyshev, and J. Knoester, "Time-dependent transport of a localized surface plasmon through a linear array of metal nanoparticles: Precursor and normal mode contributions," *Physical Review B*, Vol. 9, 085428, 2018.
16. Wu, R. P. H. and H. C. Ong, "Small mode volume topological photonic states in one-dimensional lattices with dipole-quadrupole interactions," *Physical Review Research*, Vol. 4, 023233, 2022.
17. Zhang, M.-X., Z. Zhou, L. Yan, L. Zhang, and J.-Y. Yan, "Polarization-induced topological phase transition in zigzag chains composed of metal nanoparticles," *J. Appl. Phys.*, Vol. 129, 243103, 2021.
18. Moritake, Y., M. Ono, and M. Notomi, "Far-field optical imaging of topological edge states in zigzag plasmonic chains," *Nanophotonics*, Vol. 11, No. 9, 2183–2189, 2022.

19. Zheng, J., Z. Guo, Y. Sun, H. Jiang, Y. Li, and H. Chen, "Topological edge modes in one-dimensional photonic artificial structures," *Progress In Electromagnetics Research*, Vol. 178, 1–20, 2023.
20. Sinev, I. S., I. S. Mukhin, A. P. Slobozhanyuk, A. N. Poddubny, A. E. Miroschnichenko, A. K. Samusev, and Y. S. Kivshar, "Mapping plasmonic topological states at the nanoscale," *Nanoscale*, Vol. 7, 11904, 2015.
21. Hu, P., L. Chen, A. P. Shkurinov, Y. Zhu, and S. Zhuang, "Observation of topological transmission in terahertz domino waveguide array," *IEEE Transaction of Terahertz Science and Technology*, Vol. 13, No. 4, 337–346, 2023.
22. Poddubny, A., A. Miroschnichenko, A. Slobozhanyuk, and Y. Kivshar, "Topological Majorana states in zigzag chains of plasmonic nanoparticles," *ACS Photonics*, Vol. 1, 101–105, 2014.
23. Downing, C. A. and G. Weick, "Topological collective plasmons in bipartite chains of metallic nanoparticles," *Physical Review B*, Vol. 95, 125426, 2017.
24. Bleckmann, F., Z. Cherpakova, S. Linden, and A. Alberti, "Spectral imaging of topological edge states in plasmonic waveguide arrays," *Physical Review B*, Vol. 96, 045417, 2017.
25. Ling, C. W., M. Xiao, C. T. Chan, S. F. Yu, and K. H. Fung, "Topological edge plasmon modes between diatomic chains of plasmonic nanoparticles," *Optics Express*, Vol. 23, No. 3, 2021–2031, 2015.
26. Giannini, V., G. Vecchi, and J. G. Rivas, "Lighting up multipolar surface plasmon polaritons by collective resonances in array of nanoantennas," *Physical Review Letters*, Vol. 105, 266801, 2010.
27. Solnyshkov, D. D., A. V. Nalitov, and G. Malpuech, "Kibble-Zurek mechanism in topologically nontrivial zigzag chains of polariton micropillars," *Physical Review Letters*, Vol. 116, 046402, 2016.
28. Chen, Z.-Y., L.-S. Yan, Y. Pan, L. Jiang, A.-L. Yi, W. Pan, and B. Luo, "Use of polarization freedom beyond polarization-division multiplexing to support high-speed and spectral-efficient data transmission," *Light: Science & Applications*, Vol. 6, e16207, 2017.
29. Zhou, W., M. Dridi, J. Y. Suh, C. H. Kin, D. T. Co, M. R. Wasielewski, G. C. Schatz, and T. W. Odom, "Lasing action in strongly coupled plasmonic nanocavity arrays," *Nature Nanotechnology*, Vol. 8, 506–511, 2013.
30. Wang, H., J.-W. Pan, et al., "Towards optimal single-photon sources from polarized microcavities," *Nature Photonics*, Vol. 13, 770–775, 2019.
31. Wellbrock, G. and T. J. Xia, "The road to 100G deployment," *IEEE Communications Magazine*, Vol. 48, S14, 2010.
32. Garcia-Vidal, F. J., L. Martin-Moreno, and J. B. Pendry, "Surfaces with holes in them: New plasmonic metamaterials," *J. Opt. A: Pure Appl. Opt.*, Vol. 7, S97, 2005.
33. Pros, A., E. Moreno, L. Martin-Moreno, J. B. Pendry, and F. J. Garcia-Vidal, "Localized spoof plasmons arise while texturing closed surfaces," *Physical Review Letters*, Vol. 108, 223905, 2012.
34. Shen, X. and T. Cui, "Ultrathin plasmonic metamaterial for spoof localized surface plasmons," *Laser Photonics Rev.*, Vol. 8, No. 1, 127–145, 2014.
35. Gao, Z., F. Gao, Y. Zhang, H. Xu, Y. Luo, and B. Zhang, "Forward/backward switching of plasmonic wave propagation using sign-reversal coupling," *Adv. Mater.*, Vol. 29, 1700018, 2017.
36. Gao, Z., L. Wu, F. Gao, Y. Luo, and B. Zhang, "Spoof plasmonics: From metamaterial concept to topological description," *Adv. Mater.*, Vol. 30, 1706683, 2018.
37. Yan, Q., E. Cao, Q. Sun, Y. Ao, X. Hu, X. Shi, Q. Gong, and H. Misawa, "Near-field imaging and time-domain dynamics of photonic topological edge states in plasmonic nanochains," *Nano Lett.*, Vol. 21, 9270–9278, 2021.
38. Garcia-Vidal, F. J., A. I. Fernandez-Dominguez, L. Martin-Moreno, H. C. Zhang, W. Tang, R. Peng, and T. J. Cui, "Spoof surface plasmon photonics," *Rev. Mod. Phys.*, Vol. 94, 025004, 2022.
39. Yang, Y., X. Xie, Y. Li, et al., "Radiative anti-parity-time plasmonics," *Nature Communications*, Vol. 13, 7678, 2022.
40. Yariv, A., Y. Xu, R. K. Lee, and A. Scherer, "Coupled-resonator optical waveguide: A proposal and analysis," *Optics Letters*, Vol. 24, No. 11, 711–713, 1999.

41. Li, Y., S. Xu, Z. Zhang, et al., "Polarization-orthogonal nondegenerate plasmonic higher-order topological states," *Physical Review Letters*, Vol. 130, 213603, 2023.
42. Perez-Gonzalez, B., M. Bello, A. Gomez-Leon, and G. Platero, "Interplay between long-range hopping and disorder in topological systems," *Physical Review B*, 035146, 2019.
43. Li, C. and A. E. Miroschnichenko, "Extended SSH model: Non-local couplings and non-monotonous edge states," *Physics*, Vol. 1, 2–16, 2019.
44. Chen, L., N. Xu, L. Singh, T. Cui, R. Singh, Y. Zhu, and W. Zhang, "Defect-induced Fano resonances in corrugated plasmonic metamaterials," *Adv. Optical Mater.*, Vol. 5, 1600960, 2017.
45. Gu, X., G.-D. Liu, L.-L. Wang, and Q. Lin, "Robust Fano resonance induced by topologically protected interface modes interference at gigahertz," *Appl. Phys. Express*, Vol. 15, 082004, 2022.
46. Yang, Y. and Y. Pan, "Engineering zero mode, Fano resonance, and Tamm surface states in the waveguide-array realization of the modified Su-Schrieffer-Heeger model," *Optics Express*, Vol. 27, No. 23, 32900–32911, 2019.
47. Song, F., S. Yao, and Z. Wang, "Non-Hermitian topological invariants in real space," *Physical Review Letters*, Vol. 123, 246801, 2019.
48. Wu, X., L. Wang, S. Chen, X. Chen, and L. Yuan, "Transition characteristics of Non-Hermitian Skin Effects in a Zigzag lattice without chiral symmetry," *Adv. Physics Res.*, 2300007, 2023.
49. Zhou, W.-H. and C.-X. Zhang, "Nonreciprocal Su-Schrieffer-Heeger lattice in the presence of next-nearest-neighboring coupling," *Phys. Scr.*, Vol. 98, No. 5, 055202, 2023.